ACS APPLIED NANO MATERIALS

www.acsanm.org
Article

Biomass-Based Synthesis of Tunable Photoactive Bimetallic Nanoparticles for Antibacterial and Catalytic Applications

Punsachon Jaroensin, Janistar Nunsap, Vipada Khuanchom, Bongkot Hararak, Piyangkun Lueangjaroenkit, Tawan Sooknoi, T. Randall Lee, and Pannaree Srinoi*

Cite This: ACS Appl. Nano Mater. 2025, 8, 17527−17539

ABSTRACT: The green synthesis of noble metal nanoparticles has gained increasing attention due to cost-effectiveness and environmental friendliness. This research aims to develop an efficient method to synthesize lignin-capped gold−silver nanoparticles (Li-GS NPs). Lignin has recently been reported to function both as a reducing agent and as a capping agent in the synthesis of metal nanoparticles. These Li-GS NPs were successfully synthesized via galvanic replacement by using lignin-capped silver nanoparticles (Li-Ag NPs) as a precursor. Lignin extracted from various sources, bagasse (BG), pararubber woodchip (PRW), and palm kernel shells (PKS) were used to investigate the effect of different functional group compositions on the nanoparticle formation. Li-Ag NPs were uniformly synthesized and transformed into well-dispersed Li-GS NPs via galvanic replacement with $KAuCl_4$, as indicated by an LSPR shift from 420 nm to 550−600 nm. Li-Ag NPs ranged from 8 nm to 28 nm, while Li-GS NPs exhibited a broader size distribution, reflecting gold-induced growth and morphological variation. Li-GS NPs demonstrated stronger antibacterial activity against both Gram-positive and Gram-negative bacteria, with Ag contributing significantly to bactericidal effects. Additionally, Li-GS NPs exhibited high catalytic efficiency in 4-nitrophenol reduction, completing the reaction within 1 min. Importantly, using lignin as both a reducing and a stabilizing agent is expected to significantly reduce costs and minimize the use of hazardous chemicals.

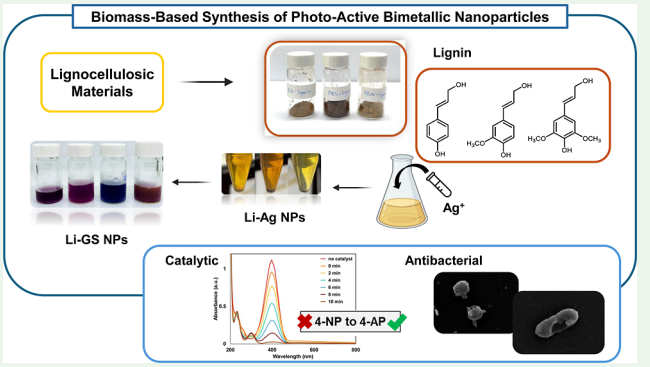

KEYWORDS: *noble metal nanoparticles, lignin, green synthesis, antibacterial, catalyst*

1. INTRODUCTION

Noble metal nanoparticles represent a fascinating class of materials that have garnered significant attention in recent decades due to their unique physical, chemical, and optical properties.[1,2] These nanoparticles, typically composed of metals, such as gold, silver, platinum, and palladium, exhibit extraordinary characteristics at the nanoscale that differ markedly from their bulk counterparts. Noble metal nanoparticles have advanced rapidly due to their wide-ranging applications in catalysis, sensing, biomedical application, and environmental remediation.[3,4] The attributes of these nanoparticles, including their small size, high surface-area-to-volume ratio, and tunable optical properties, contribute to their exceptional versatility, rendering them suitable for a wide array of technological innovations. These tiny structures, frequently demonstrating remarkable biocompatibility, possess the capacity to interact with biological systems in highly sophisticated ways. While noble metal nanoparticles are made of one type of noble metal, bimetallic nanoparticles are a subset that contains two metal elements, which can include noble metals. Bimetallic nanoparticles are designed to combine the properties of the two metals or create new properties that neither metal possesses alone.[5−7]

Silver nanoparticles (Ag NPs) have been used in a variety of applications due to their unique features, such as catalytic, sensing, and antibacterial properties. Ag NPs have become the focus of attention in the biomedical area as pathogenic bacteria have developed antibiotic resistance, resulting in many severe and chronic diseases and fatalities.[8,9] Bacteria cannot acquire resistance to Ag NPs due to their characteristics. However, in terms of colloidal stability, gold nanoparticles (Au NPs) are thought to be more stable than other noble metal nanoparticles. Because of their great stability and biocompatibility, Au NPs have been reported to be used in a variety of biological applications.[10−12] As a result, this combination of two noble metals in bimetallic gold−silver nanoparticles has great

Received: June 25, 2025
Revised: August 20, 2025
Accepted: August 22, 2025
Published: September 3, 2025

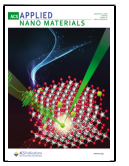

Scheme 1. Synthesis of Li-GS NPs Using Li-Ag NPs as Templates

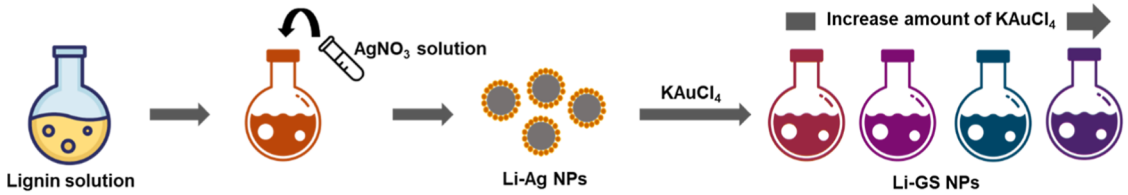

potential for utilization for a range of biomedical applications, including photothermal and antibacterial ones.[13]

Generally, noble metal nanoparticles have been synthesized using strong reducing agents such as sodium borohydride ($NaBH_4$), and trisodium citrate ($Na_3C_6H_5O_7$), which are costly and nonenvironmentally friendly.[14,15] To overcome the mentioned issue, green synthesis of nanomaterials has been utilized as a promising method due to the reduction of hazardous chemicals used in the synthesis process. This ecofriendly synthesis process not only avoids the use of chemicals but also reduces the amount of hazardous waste. Specifically, green synthesis of metal nanoparticles has been achieved by various natural materials such as bacteria, fungi, algae, and plant extracts.[16−19]

Lignocellulosic biomass is a plant-derived material that consists of cellulose, hemicellulose, and lignin. Lignin has been generally discarded as a waste byproduct of the lignocellulosic biomass pulping process in the paper-making industry and the biorefinery process. In comparison to other agricultural waste components, the use of lignin requires further investigations. In terms of structure, lignin is a polymeric molecule that contains aromatic phenolic and methoxy phenolic units. Lignin subunits consist of coumaryl alcohol (H unit), coniferyl alcohol (G unit), and sinapyl alcohol (S unit).[20−22] In addition, lignin can be briefly classified into three types, including softwood lignin, hardwood lignin, and herbaceous/grass lignin. Based on the ratio of monomers, the softwood lignin contains mainly the G unit, the hardwood lignin has both G and S units, and the herbaceous lignin has all three monomer units. Therefore, the difference in its composition may affect both physical and chemical properties which leads to the specific potential applications for each isolated lignin.[23,24]

Regarding the synthesis of noble metal nanoparticles, lignin can be used as a reducing agent and a capping agent due to its electron donating groups such as the hydroxy group (−OH) and methoxy group (OCH_3). Lignin has been reported to enhance the colloidal stability of metal nanoparticles in aqueous solutions.[25] Thus, lignin is an alternative source that served as a green reducing, capping, and stabilizing agent in nanoparticles synthesis.[26,27] Additionally, gold−silver nanoshells and lignin-based nanoparticles separately have been reported to exhibit the crucial antibacterial effects.[28−31] Moreover, various metal nanoparticles have been reported as a catalyst for a wide range of reactions.[32−35] However, several challenges remain in the green synthesis of metal nanoparticles. One major issue is controlling the morphology, as green reducing agents like lignin often lead to broad size distributions and irregular shapes due to the variability in their molecular structure and reactivity.[36] Therefore, the development of a reliable and environmentally friendly synthesis strategy that allows for better control over the nanoparticle morphology, composition, and stability is of critical importance and forms the basis of the present study. Herein, in this project, we aim to modify the synthesis of lignin-capped gold−silver nanoshells (Li-GS NPs) to limit the use of hazardous chemicals, especially strong reducing agents for the synthesis of metal nanoparticles. In the modifying method, lignin can be used as both reducing and capping agents. Moreover, the lignin extracted from various agricultural wastes was used to study the effect of various ratios of functional groups on metal nanoparticles synthesis. In this study, bagasse, pararubber woodchip, and palm kernel shells were selected for their abundance as agricultural residues and their specific physical and chemical properties. The compositional differences can significantly influence lignin's reducing and capping abilities during nanoparticle synthesis. However, the influence of lignin source variability on noble metal nanoparticle formation remains largely unexplored. The synthesized Li-GS NPs are expected to maximize the advantage of the nanocomposites in antibacterial and catalytic applications.

2. EXPERIMENTAL SECTION

2.1. Materials. Three types of lignin, pararubber woodchip (PRW) lignin, palm kernel shell (PKS) lignin, and bagasse (BG) lignin, were utilized in this study. All lignin samples were kindly provided by the National Center for Genetic Engineering and Biotechnology (BIOTEC, NSTDA, Thailand). All lignin types were obtained via organosolv pretreatment, resulting in high-purity lignin with a content greater than 90%. Potassium tetrachloroaurate (III) ($KAuCl_4$) was acquired from Sigma-Aldrich and Thermo Scientific Chemicals. Silver nitrate ($AgNO_3$T) and sodium hydroxide (NaOH) were obtained from Merck (Germany). Hydrochloric acid (HCl, 37%) was supplied by Quality Reagent Chemical. Sodium borohydride ($NaBH_4$, ≥98%) and 4-nitrophenol ($C_6H_5NO_3$) were purchased from Tokyo Chemical Industry (TCI). All reagents were of analytical grade and used without additional purification.

2.2. Characterizations of Lignin. In this study, there are three distinct types of lignin: bagasse-extracted lignin (BG), pararubber woodchip-extracted lignin (PRW), and palm kernel shell-extracted lignin (PKS). These lignin samples were derived via an organosolv pretreatment method, resulting in high-purity lignin (>90%) with minimal residual sugar contamination. The organosolv process, detailed in previous publications, effectively fractionates the lignocellulosic biomass, yielding the lignin with specific structural characteristics influenced by the source material and processing conditions.[37] Additionally, ^{31}P NMR spectroscopy was used for quantitative identification of functional groups in each lignin structure. Lignin samples were dried in a vacuum oven at 45 °C for 24 h to remove moisture from the structure. The dried samples were dissolved in a mixture of 2.5 mL of deuterated chloroform and 4 mL of anhydrous pyridine prior to the analysis.

2.3. Synthesis of Silver Nanoparticles (Li-Ag NPs). Li-Ag NPs were synthesized by using three different types of extracted lignin as reducing agents. Specifically, 20 mM of aqueous solution of $AgNO_3$ was prepared by dissolving 0.0167 g (10 mmol) in 5 mL of ultrapure water. Separately, 45 mL of selected concentrations of lignin aqueous solution was heated to the specific temperature. Five milliliters of as-prepared $AgNO_3$ solution were added to heated lignin solution under stirring conditions. The reaction mixture was refluxed for 150 min. The reaction mixture was cooled to room temperature. The resulting nanoparticles were collected by centrifugation at 10,000 rpm for 15

https://doi.org/10.1021/acsanm.5c03025
ACS Appl. Nano Mater. 2025, 8, 17527−17539

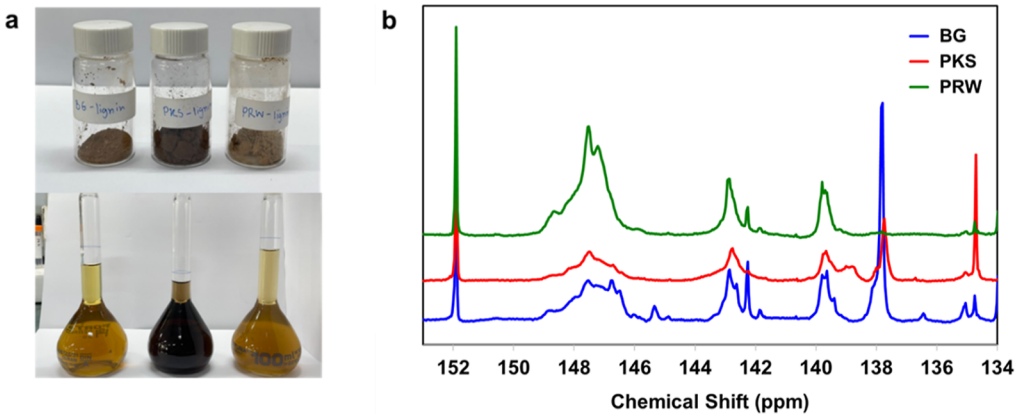

Figure 1. (a) Dried lignin and lignin aqueous solution and (b) quantitative ^{31}P NMR spectra of BG-, PRW-, and PKS-lignin.

min and then redispersed in ultrapure water. The colloidal nanoparticles were stored at 4 °C prior to further experiments and analyses.

2.4. Synthesis of Lignin-Coated Hollow Gold−Silver Nanoparticles (Li-GS NPs). The as-prepared Li-Ag NPs were used as a template to synthesize lignin-coated gold−silver nanoparticles (Li-GS NPs). The synthesis scheme for Li-GS NPs is presented in Scheme 1. Specifically, 50 mL of a Li-Ag NPs solution was mixed with various amounts of $HAuCl_4$ solution. The reaction was kept at room temperature under stirring conditions for 2 days. The change of optical property was monitored every 1 h using an UV−visible spectrophotometer. The product was collected using centrifugation at 10,000 rpm for 15 min and redispersed in ultrapure water. The colloidal Li-GS NPs solution was stored at 4 °C.

2.5. Characterizations of Nanoparticles. The extinction spectra for all experiments were measured by using a double-beam UV−visible spectrophotometer (UV/vis Lambda 365, PerkinElmer). The localized surface plasmon resonance (LSPR) spectra of all Li-Ag NPs and Li-GS NPs samples were recorded in the wavelength range of 200 to 800 nm, with a spectral bandwidth (SBW) of 1 nm and a scan speed of 10 nm/s. The morphology and size distribution of Li-Ag NPs and Li-GS NPs were further investigated by using a field emission transmission electron microscope (FE-TEM) (JEOL JEM-3100F) operated at 200 kV. High-resolution TEM (HR-TEM) imaging provided detailed structural information, including lattice fringes indicative of crystallinity, while selected area electron diffraction (SAED) patterns were obtained to confirm the crystalline phase of the synthesized nanoparticles. For TEM sample preparation, the nanoparticles were first sonicated for 5 min to ensure a uniform dispersion. A 20 μL portion of the nanoparticle suspension was dropped onto a carbon-coated copper grid and left to dry overnight prior to the analysis. The hydrodynamic particle size distribution and surface charge (zeta potential) of Li-Ag NPs and Li-GS NPs were measured using a Zetasizer Ultra (Malvern Panalytical) via dynamic light scattering (DLS) and electrophoretic light scattering (ELS), respectively. Prior to zeta potential measurements, the samples were diluted to a final concentration of 10 mg/mL to minimize interparticle interactions that could affect the measurement accuracy. The chemical structure and functional groups of lignin and Li-Ag NPs were analyzed by using attenuated total reflectance Fourier-transform infrared (ATR-FTIR) spectroscopy. ATR-FTIR spectra were collected on a PerkinElmer Spectrum Two Fourier-transform infrared spectrometer.

2.6. Antibacterial Properties Tests. The antibacterial activity of the as-prepared nanoparticles was evaluated against Gram-positive *Bacillus cereus* ATCC 14579 and *Staphylococcus aureus* ATCC 29213 and Gram-negative *Escherichia coli* ATCC 8739. Minimum inhibitory concentration (MIC) testing was conducted using a 96-well microdilution method, following the protocol.[38] Bacterial inoculum was prepared using Mueller−Hinton (MH) agar. Serial 2-fold dilution of Li-Ag NPs and Li-GS NPs in final concentration ranging from 20 to 0.1 μg/mL with adjusted bacterial suspension (standard turbidity of 0.5 McFarland; 1.5×10^8 CFU/mL were used to determine MIC in MH broth). The plates were incubated for 24 h at 37 °C. The bacterial turbidity was measured at 660 nm using a microplate reader (Multiskan GO Microplate Spectrophotometer, Thermo Fisher Scientific, USA), and thereafter, the MIC was determined. The MIC end point is the lowest concentration of nanoparticles where no bacterial growth was observed. A microdilution measurement was done in triplicate to confirm the value of the MIC for each tested bacterium. Following the MIC determination, the minimum bactericidal concentration (MBC) was assessed. Two microliters from wells showing no visible growth were cultured on MH agar plates and incubated for 24 h at 37 °C. MBC was defined as the lowest concentration of nanoparticles that resulted in the death of 99.9% of the bacterial inoculum.

The size and morphology of bacteria before and after exposure to Li-Ag NPs were analyzed using a FEI Quanta 450 scanning electron microscope (SEM) operated at an accelerating voltage of 25.00 kV in the 500× to 5000× magnification range under secondary electron (SE) mode. To improve the electrical conductivity and enhance imaging resolution, a thin layer of gold was sputter-coated onto all bacterial samples using a Polaron Range SC7620 Sputter Coater (Quorum Technology) prior to SEM analysis.

2.7. Catalytic Performance Test. The catalytic activity of the synthesized nanoparticles was evaluated using the reduction of 4-nitrophenol (4-NP) to 4-aminophenol (4-AP) in the presence of sodium borohydride ($NaBH_4$) to assess the nanoparticles' catalytic activities.[39] The synthesized Li-GS NPs catalysts were employed at four different concentrations. A 0.1 M $NaBH_4$ solution was prepared by dissolving the appropriate amount of $NaBH_4$ in ultrapure water. The influence of catalyst quantity on the reduction of 4-NP was investigated using UV−visible spectrophotometry, with absorbance measurements taken for reactions consisting of 2 mL of 4-nitrophenol, 200 μL of $NaBH_4$, and catalyst volumes of 10, 20, and 30 μL. This experiment was conducted for each of the synthesized Li-GS NPs catalyst concentrations.

3. RESULTS AND DISCUSSION

3.1. Characterizations of Lignin. The dried lignin samples and their aqueous solutions from the three sources showed slightly different colors, as illustrated in Figure 1a. All samples appeared dark yellow or brown. These small color differences were confirmed by the UV−visible absorption spectra in Figure S1 in the Supporting Information, which vary depending on the plant source.[40] The maximum absorbance wavelengths (λ_{max}) of PKS-, BG-, and PRW-lignin were found at 289, 285, and 281 nm, respectively, as summarized in Table S1. These absorption peaks are caused by π-to-π^* electronic transitions, which are typical for all lignin types. Additionally.

https://doi.org/10.1021/acsanm.5c03025
ACS Appl. Nano Mater. 2025, 8, 17527−17539

^{31}P NMR was used to determine the number of total hydroxyl groups in lignin. All types of lignin were successfully phosphorylated by ^{31}P in TMDP in which ^{31}P substituted hydrogen (H) at the −OH position. The different hydroxyl groups were quantified and distinguished with ^{31}P NMR spectra as shown in Figure 1b. The quantitative spectra showed the different chemical shifts of each lignin functional group in all types of lignin, and the chemical shift range to identify each functional group is shown in Table S2 in the Supporting Information. According to the results shown in Table 1, BG-, PRW-, and PKS-lignin contain total amounts of hydroxyl groups of 5.67, 7.02, and 7.35 mmol/g, respectively.

Table 1. Hydroxyl Groups (−OH) in BG-Lignin, PRW-Lignin, and PKS-Lignin

OH group		OH contents (mmol/g)		
		BG-lignin	PRW-lignin	PKS-lignin
aliphatic OH		1.92	3.93	2.22
phenolic OH	C_5 substituted OH	1.11	1.30	1.46
	syringyl OH	0.60	0.68	0.78
	guaiacyl OH	0.59	0.66	0.85
	p-hydroxyphenyl OH	1.09	0.08	0.70
total amount phenolic OH		3.39	2.72	3.79
carboxylic acid OH		0.36	0.37	1.34
total amount of OH		5.67	7.02	7.35

Specifically, BG- and PKS-lignin mainly consist of phenolic hydroxyl groups, while PRW-lignin contains mostly aliphatic −OH groups. The various types and content of hydroxyl groups may affect the rate of Ag NPs synthesis due to the difference of electron donation groups.

Lignin's chemical reactivity and functional performance can vary significantly depending on its botanical origin and extraction method, which influence its structural composition, molecular weight, and functional group distribution.[41] Phenolic −OH groups, particularly those attached to aromatic units, are the primary electron donors responsible for reducing Ag^+ to Ag^0 under mild conditions. Chemical structures of hydroxyl groups in lignin are illustrated in Figure S2 in the Supporting Information. Among these, syringyl (S) units, which possess two methoxy substituents on the aromatic ring, exhibit the highest electron density and are generally the most effective in donating electrons due to their enhanced resonance stabilization.[42] Guaiacyl (G) units, containing a single methoxy group, are also redox-active but slightly less efficient than syringyl structures. In contrast, p-hydroxyphenyl (H) units, which lack methoxy substituents, offer limited electron delocalization and therefore exhibit a weaker reducing capability. Additionally, C_5-substituted phenolic OH groups, commonly found in condensed G-type structures, are often sterically hindered or involved in cross-linking, which can limit their accessibility for redox reactions.[43] Meanwhile, aliphatic −OH groups, present on lignin side chains, are less redox-active

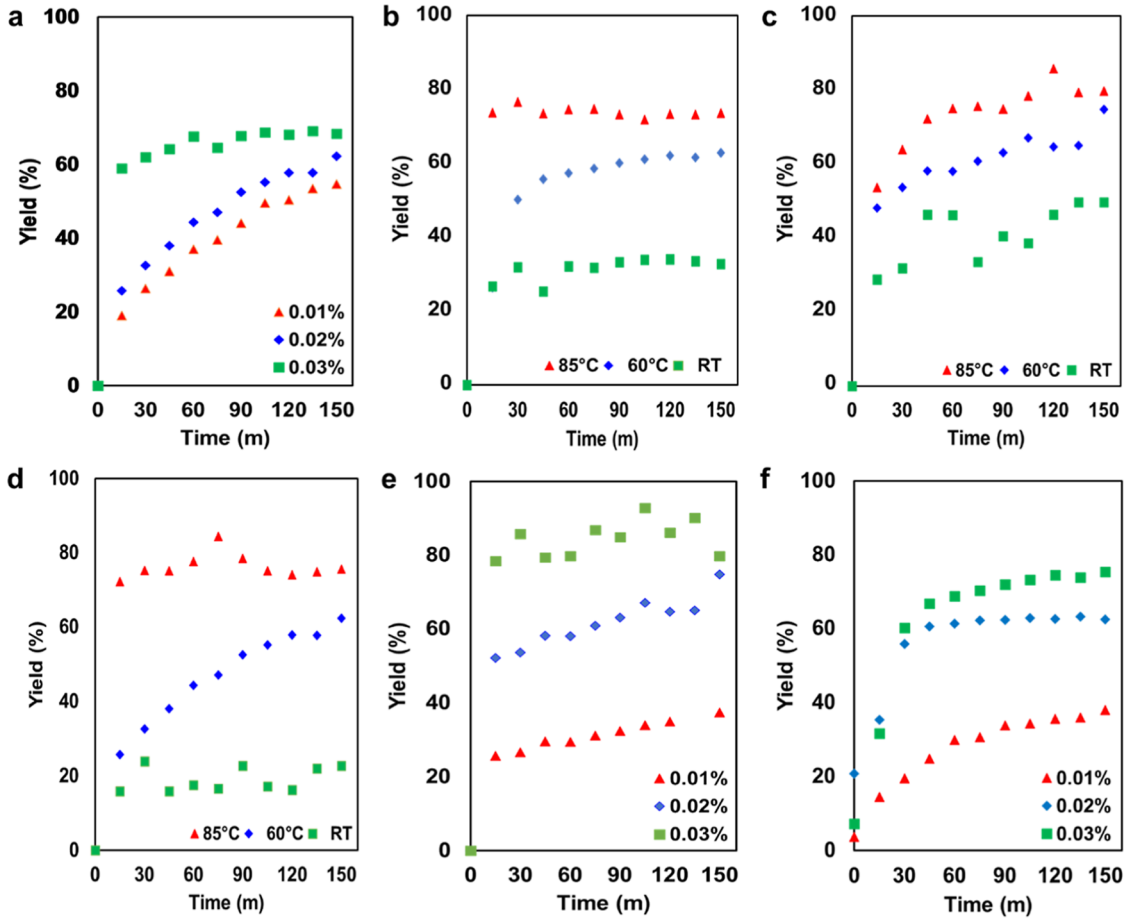

Figure 2. % Yield of Ag NPs synthesized with 0.02% w/v: (a) PKS-lignin, (b) PRW-lignin, and (c) BG-lignin at various temperatures, and synthesized various concentrations of (d) PKS-lignin, (e) PRW-lignin, and (f) BG-lignin.

https://doi.org/10.1021/acsanm.5c03025
ACS Appl. Nano Mater. 2025, 8, 17527−17539

but contribute indirectly by improving lignin solubility, dispersion, and molecular flexibility in aqueous environments, which, in turn, influences the uniformity of nanoparticle growth. In this study, lignin samples with higher ratios of syringyl and guaiacyl −OH (e.g., from bagasse and pararubber wood) promoted more efficient and uniform Ag NP synthesis, while lignin from palm kernel shell, despite having the highest total phenolic −OH content, showed lower efficiency likely due to structural condensation, higher proportions of C_5-substituted units, and less favorable solubility behavior.

The effectiveness of lignin in reducing Ag^+ to Ag^0 during nanoparticle synthesis is closely related to its phenolic structure and functional group distribution. Among the phenolic subunits, syringyl and guaiacyl groups differ in reactivity due to their degree of methoxylation, with syringyl (bearing two methoxy groups) being more electron-rich and more reactive than guaiacyl groups (with one methoxy group). The p-hydroxyphenyl units, which lack methoxy groups, are generally less reactive, and C_5-substituted OH groups, especially in condensed lignin structures, tend to be sterically hindered and less available for redox reactions. Interestingly, although PKS lignin showed the highest total phenolic −OH content (3.79 mmol/g), it did not produce the highest Ag NP formation efficiency. This unexpected behavior may be attributed to the limited accessibility of reactive phenolic sites, possibly due to higher structural condensation, intramolecular hydrogen bonding, or steric hindrance from C_5-substituted guaiacyl units. In contrast, BG and PRW lignin, with lower phenolic −OH content (3.39 and 2.72 mmol/g, respectively), achieved better reduction efficiency. One contributing factor may be the higher aliphatic −OH content in PRW lignin (3.93 mmol/g), which, while not directly reducing Ag^+, likely improves solubility, molecular flexibility, and nanoparticle stabilization in aqueous media. These findings suggest that not only the amount but also the type and accessibility of hydroxyl groups in lignin significantly influence the nanoparticle formation process. While phenolic −OH groups are the primary reducing agents for Ag^+, aliphatic −OH groups play a supportive role by influencing the solubility, molecular mobility, and nanoparticle stabilization ability of lignin. In PRW lignin, the high aliphatic −OH content may enhance lignin−metal interactions and nanoparticle dispersion, partially compensating for its lower phenolic content.[44] In contrast, PKS lignin, despite its high phenolic −OH content, may be less efficient due to the lower aliphatic −OH, resulting in reduced flexibility and site accessibility.

3.2. Synthesis of Li-Ag NPs. Temperature is an important factor that influences the synthesis of nanoparticles. In the synthesis of silver nanoparticles using lignin extracts at varying temperatures of 85 °C, 60 °C, and room temperature, an increase in temperature was observed to increase the rate of the reduction of Ag^+ ions by lignin. Figure 2 illustrates the percentage yields of Ag NPs at different temperatures. These figures clearly demonstrate the effect of the temperature on the synthesis process. At 85 °C, the rapid completion of the reaction was achieved within 15−45 min for all types of lignin. The result suggests a highly efficient reduction process facilitated by high thermal energy, which enhances the kinetics of the reaction. At 60 °C, the reaction proceeds at a moderate rate, with a steady increase in nanoparticle formation observed over 150 min. This temperature provides a balance between reaction rate and control over the nanoparticle size and distribution. At room temperature, the synthesis of silver nanoparticles is obviously slower and shows a lower concentration of Ag NPs. This indicates that higher temperatures promote faster formation of silver nanoparticles more effectively than lower temperatures. A high temperature significantly enhances the rate of the reduction reaction, leading to a fast and efficient nanoparticle formation. However, the choice of temperature must be balanced with the desired properties of the nanoparticles, such as size, uniformity, and stability, to optimize the synthesis process for specific applications.

From the synthesis of Li-Ag NPs using lignin extracts at different concentrations of 0.01%, 0.02%, and 0.03% by weight, it was observed that the percentage yields of PKS-Ag NPs at a reaction time of 150 min were 54.67%, 62.35%, and 68.41%, respectively, for lignin concentrations of 0.01%, 0.02%, and 0.03% by weight. The percentage yields of PRW-Ag NPs at the same reaction time were 37.37%, 74.77%, and 79.76%, respectively, for lignin concentrations of 0.01%, 0.02%, and 0.03% by weight. The percentage yields of BG-Ag NPs at the same reaction time were 37.93%, 54.22%, and 75.28%, respectively, for lignin concentrations of 0.01%, 0.02%, and 0.03% by weight. The experimental results indicate that a lignin solution at a concentration of 0.01% produces fewer silver nanoparticles compared with concentrations of 0.02% and 0.03%. At low lignin concentration (0.01%), the availability of reducing agents is limited, resulting in a lower rate of Ag^+ ion reduction and small size of the nanoparticles, as shown in Figure S3a. As the concentration increases to 0.02% and 0.03%, the number of agents increases, enhancing the reduction process and resulting in a higher yield and larger size of Ag NPs, as illustrated in Figure S3b,c, respectively. The stabilization of the nanoparticles is also improved at higher lignin concentrations, which helps in maintaining a uniform size and preventing agglomeration.

Fourier Transform Infrared (FT-IR) spectroscopy showed the spectra data from lignin pyrolysis provide a comprehensive analysis of the functional groups present in lignin derived from pararubber wood (PRW), palm kernel shell (PKS), and bagasse (BG). The FT-IR spectra, as shown in Figure S4 in the Supporting Information, revealed that the different functional groups exhibited vibrations, and common absorption peaks across all lignin samples, indicating the presence of hydroxyl groups at 3425 cm^{-1}, methyl/methylene groups which is the signal of C−H stretching in CH_2 and CH_3 groups at 2920 cm^{-1}, carbonyl groups at 1710 cm^{-1}, and aromatic rings at 1600, 1510, and 1430 cm^{-1}.[27] These peaks indicate the structural components typical of lignin including hydroxyl, methylene, carbonyl, and aromatic functionalities. The fingerprint regions of the FTIR spectra showed specific characteristics for different lignin types. For instance, softwood lignin, such as those from pararubber wood, exhibited C−O stretching peaks of guaiacyl units at 1270 cm^{-1} and 1215 cm^{-1}, while hardwood lignins, such as those from palm shell, displayed additional peaks of syringyl units at 1120 $cm^{-1}$and 1325 cm^{-1}.[45,46] Bagasse lignin, which is grass lignin, also showed signals of both guaiacyl and syringyl units, albeit with lower intensities. The relative intensities of hydroxyl, methyl/methylene, and carbonyl groups were calculated using the aromatic ring peak at 1510 cm^{-1} as reported earlier.[47] This study highlighted variations in the abundance of these functional groups across different lignin sources, reflecting

https://doi.org/10.1021/acsanm.5c03025
ACS Appl. Nano Mater. 2025, 8, 17527−17539

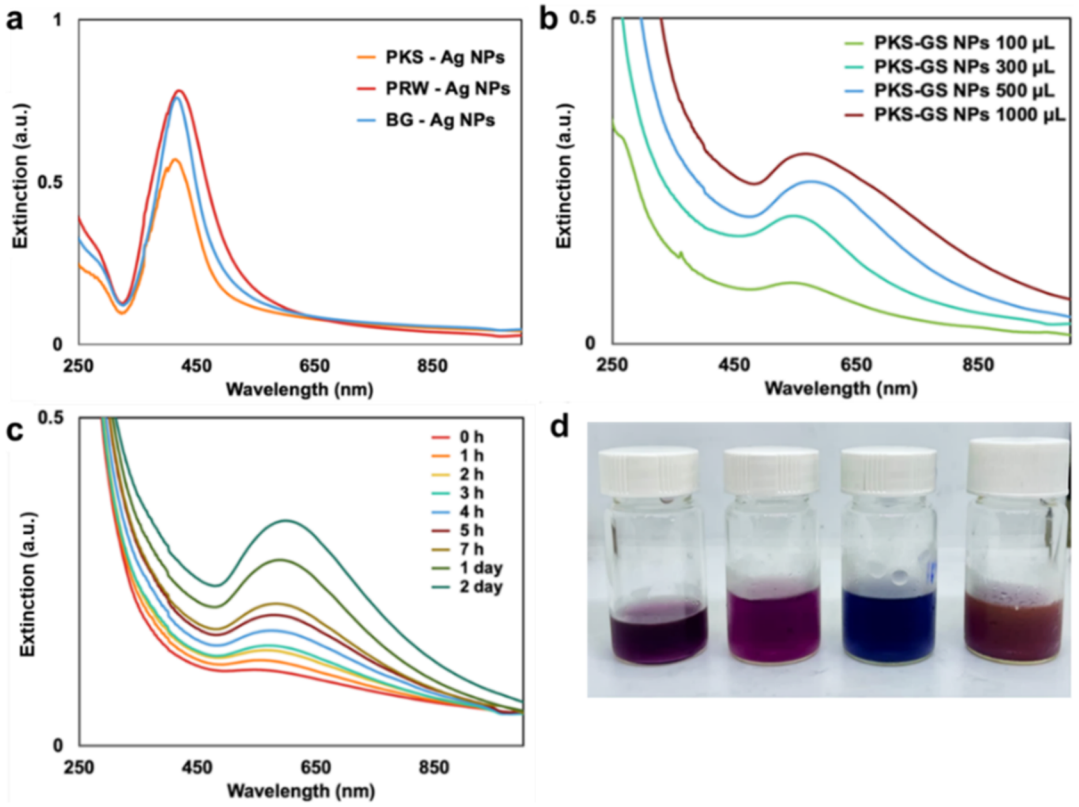

Figure 3. (a) Extinction spectra of Li-Ag NPs. (b) Extinction spectra and (d) images of Li-Ag NPs solution after the addition of various amounts of $KAuCl_4$. (c) Extinction spectra of Li-Ag NPs solution after the addition of $KAuCl_4$ from 0 h to 2 days.

their structural diversity and potential reactivity during the reduction process.

The synthesis of metal nanoparticles, particularly Ag NPs, using lignin as both a reducing and stabilizing agent follows a well-defined mechanistic pathway involving redox chemistry, nucleation, growth, and capping. Lignin, a heterogeneous aromatic biopolymer composed mainly of syringyl (S), guaiacyl (G), and p-hydroxyphenyl (H) units, contains a variety of redox-active functional groups, such as phenolic hydroxyls, aliphatic hydroxyls, methoxyls, and occasionally carboxyl groups. Among these, phenolic −OH and benzylic $-CH_2OH$ groups are the primary electron donors responsible for reducing metal ions like Ag^+ or Au^{3+} to their zerovalent metallic forms.[48] The mechanism begins with the complexation of metal ions with electron-rich sites on lignin, typically through coordination with phenolic hydroxyls or π-interactions with aromatic rings. In this initial step, the metal ions become localized within the lignin matrix, creating favorable conditions for controlled nucleation.

Once coordinated, redox reactions are initiated, and phenolic −OH groups are oxidized to quinone-like structures while reducing Ag^+ to Ag^0. Likewise, $-CH_2OH$ groups may undergo oxidation to aldehydes or acids. In cases where lignin is chemically modified, such as through amination, the presence of $-NH_2$ groups offers an additional redox pathway. These groups can be oxidized to imines or nitriles during the reaction, leading to a more effective electron transfer, enhanced reduction kinetics, and higher nanoparticle yields. Following reduction, nucleation of Ag^0 atoms occurs, forming small clusters that serve as growth centers. The subsequent growth phase involves the deposition of more reduced atoms onto these nuclei, guided by the availability of reducing groups and the steric environment within the lignin matrix. Lignin with higher phenolic content and lower C_5 substitution tend to promote uniform nucleation and narrower size distributions, while condensed lignin or those with limited functional group accessibility may lead to particle aggregation or polydispersity.[49,50] Finally, lignin plays a vital role in capping and stabilizing the newly formed nanoparticles. Unreacted functional groups, such as phenols, carboxylic acids, or amines, adsorb onto the nanoparticle surfaces, preventing agglomeration through steric hindrance and electrostatic repulsion. This natural capping effect improves the colloidal stability and dispersibility of the nanoparticles in aqueous media.

3.3. The Synthesis of Li-GS NPs. The formation of Li-Ag NPs was easily detected by a noticeable color change in the solution, which transitioned from colorless to light yellow after the addition of lignin. This color change serves as an indication that silver ions (Ag^+) were reduced to metallic silver (Ag^0) or Ag NPs by the lignin. The synthesized Li-Ag NPs were also characterized by UV−visible spectroscopy to identify the characteristic peak of Ag NPs at 420 nm. The reaction was carried out using the synthesis procedure as mentioned previously. As shown in Figure 3a, Ag NPs synthesized with PKS, PRW, and BG lignin exhibited a characteristic peak of Ag NPs which confirm the formation of Ag NPs using lignin as a reducing agent. The LSPR absorption peaks of Ag NPs synthesized with all types are observed in the 410−430 nm range, as concluded in Table S3 in the Supporting Information. These peaks confirm the formation of Li-Ag NPs, with lignin acting as an effective capping and reducing agent. Additionally, BG- and PRW-Ag NPs exhibit the sharpest and most symmetric extinction peaks, indicating a narrower particle size distribution and the presence of monodisperse Ag NPs. In

https://doi.org/10.1021/acsanm.5c03025
ACS Appl. Nano Mater. 2025, 8, 17527−17539

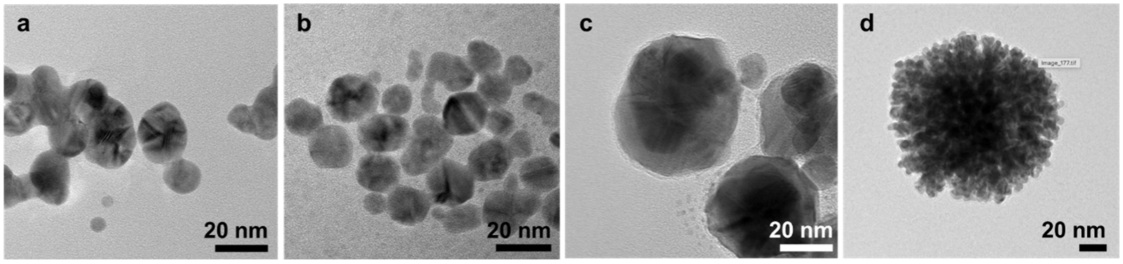

Figure 4. TEM images of (a) PKS-GS NPs-100, (b) PKS-GS NPs-300, (c) PKS-GS NPs-500, and (d) PKS-GS NPs-1000.

contrast, the LSPR peaks of PKS-Ag NPs show less extinction intensity, which indicates the lower quantity of Ag NPs.[36] This observation is consistent with the ^{31}P NMR analysis, which shows that PKS-lignin contains the highest proportion of the guaiacyl OH group. The G monomer unit, rich in both hydroxyl and methoxy groups, exhibits strong reducing properties, enabling it to easily donate electrons to Ag^+ in redox reactions. The oxidation of both phenolic and alcoholic hydroxyl groups in lignin leads to the formation of quinone, carbonyl, and carboxyl groups. This process primarily occurs through alcoholic oxidation, converting the alcoholic hydroxyl groups into carbonyl groups, which can further be oxidized into carboxyl groups, while the phenolic hydroxyl groups undergo oxidation to form quinones.[51] Additionally, PKS-lignin's highly uniform polymeric structure may contribute to the sharp, symmetrical absorption peak observed in PKS-Ag NPs. Typically, the λ_{max} of Ag NPs shifts toward longer wavelengths (red shift) as the particle size increases.[52]

All of the as-prepared Li-Ag NPs were used as a template to synthesize Li-GS NPs. The different amounts of $KAuCl_4$ (100, 300, 500, and 1000 μL) have been used to synthesize the PKS-GSNPs to find the optimizing condition. The amount of the $KAuCl_4$ solution plays a critical role in controlling the synthesis and structural evolution of Li-GS NPs. As the volume of $KAuCl_4$ increases, a greater number of Au^{3+} ions are introduced into the reaction system, which enhances the galvanic replacement of Ag atoms by Au.[53] This process leads to the gradual formation of Au-Ag bimetallic nanostructures, with varying degrees of alloying or core−shell configurations depending on the amount of gold precursor added. From Figure 3b, at a lower amount of 1% w/v $KAuCl_4$ (100 μL), the galvanic replacement appears to be partial, resulting in a low-intensity gold characteristic peak. In contrast, higher volumes promote more complete substitution of silver by gold, shifting the composition toward gold-rich alloys. As a result, the optical properties of the synthesized nanoparticles, as observed by UV−visible spectroscopy, vary with the volume of $KAuCl_4$ added, often exhibiting a red shift and broadening of the LSPR band. At a volume of 1,000 μL $KAuCl_4$, both BG-GS NPs and PKS-GSNPs show the highest absorbance intensity and exhibit less symmetrical or right-skewed spectral profiles. This asymmetry is attributed to gold's interband transitions in the 500−600 nm range, which absorb and dampen the plasmonic oscillations, resulting in a broader tail on the longer wavelength side and enhancing the right skew of the spectrum.[53] However, for PRW-GS NPs in the same volume (1000 μL), the LSPR spectrum shows a significantly broadened peak and a pronounced shift toward longer wavelengths. This behavior is likely due to size and morphology effects specifically the presence of larger or nonspherical particles such as hollow shells, rods, or aggregates which support multiple plasmon modes and contribute to additional spectral broadening.[54] These spectral shifts indicate changes in particle composition, morphology, and electronic structure, emphasizing the importance of $KAuCl_4$ volume in tuning the properties of Li-GS NPs.[55]

The optimizing time of all Li-GS NPs preparation was identified by collecting and measuring the extinction peak of the samples from the reaction at 1 h until 2 days. As shown in Figure 3c, after 3 h of reaction, the extinction peak of PKS-GS NPs appeared at 615 nm and remained at 565 nm until 7 h. After 1 day of reaction, the extinction peak of PKS-GS NPs-300 was slightly shifted to longer wavelength at 570 nm. The extinction intensity of the extinction peak was significantly increased from the reaction at 7 h. However, after the reaction was left at room temperature for 2 days, the extinction peak position and intensity was slightly changed from the reaction at 1 day. From this observation, the optimizing time of the synthesis of Li-GS NPs was selected to be 24 h due to the maximum change in optical properties of the as-prepared nanoparticles. Additionally, the galvanic replacement reaction is employed to synthesize Li-GS NPs with various morphologies. This process is driven by the difference in reduction potentials between gold and silver. During the galvanic replacement reaction between Ag and Au, silver atoms in the nanostructure are oxidized to Ag^+ and released into the solution. Simultaneously, Au^{3+} is reduced and deposited onto the silver template. This redox process leads to the formation of Au/Ag alloy nanostructures due to the difference in reduction potentials between the two metals, as shown in eqs S1−S3 in the Supporting Information. This reaction causes the color of the Li-Ag NPs solution to change from pale yellow to purple or blue upon completion, as shown in Figure 3d. The color of the nanoparticles is primarily influenced by their composition, specifically the gold-to-silver ratio. This ratio affects the nanoparticles' localized surface plasmon resonance (LSPR), leading to observable color changes.[56,57]

TEM images of the as-prepared PKS-GS NPs are presented in Figure 4. The TEM images also corroborate the nanoscale nature of the particles, further validating the size estimations. This inconsistency arises from the etching and redeposition of metal during the synthesis process, which induces significant morphological variation. TEM measurements of the average sizes of Li-Ag NPs indicated a size range of 8−28 nm. In contrast, the sizes of Li-GS NPs were shown to increase with the progressive addition of the $KAuCl_4$ solution to the reaction, demonstrating a direct correlation between the gold content and particle size. Specifically, the PKS-GS NPs exhibited average sizes of 16.64 ± 3.86 nm, 15.54 ± 7.74 nm, 34.32 ± 18.09 nm, and 100.95 ± 37.58 nm for PKS-GS NPs-100, PKS-GS NPs-300, PKS-GS NPs-500, and PKS-GS NPs-1000, respectively. This trend was also observed in PRW-

https://doi.org/10.1021/acsanm.5c03025
ACS Appl. Nano Mater. 2025, 8, 17527−17539

Table 2. MIC and MBC Values of Li-Ag NPs against the Selected Bacteria

	Bacillus cereus		*E. coli*		*S. aureus*	
nanoparticles	MIC (μg/mL)	MBC (μg/mL)	MIC (μg/mL)	MBC (μg/mL)	MIC (μg/mL)	MBC (μg/mL)
PKS-Ag NPs	20	>20	>20	>20	20	>20
PKS-GS NPs-100	2.5	5	10	10	5	5
PKS-GS NPs-300	1	2.5	10	10	1	2.5
PKS-GS NPs-500	0.5	1	5	5	1	2.5
PKS-GS NPs-1000	2.5	5	5	2.5	0.5	1
PRW-Ag NPs	20	>20	>20	>20	20	>20
PRW-GS NPs-100	1	5	10	10	0.5	2.5
PRW-GS NPs-300	5	10	5	10	0.5	2.5
PRW-GS NPs-500	5	10	2.5	5	1	2.5
PRW-GS NPs-1000	1	2.5	5	10	1	5
BG-Ag NPs	20	>20	>20	>20	10	20
BG-GS NPs-100	2.5	5	20	20	5	5
BG-GS NPs-300	5	10	10	5	0.5	2.5
BG-GS NPs-500	1	2.5	5	10	0.5	2.5
BG-GS NPs-1000	2.5	1	5	10	1	2.5

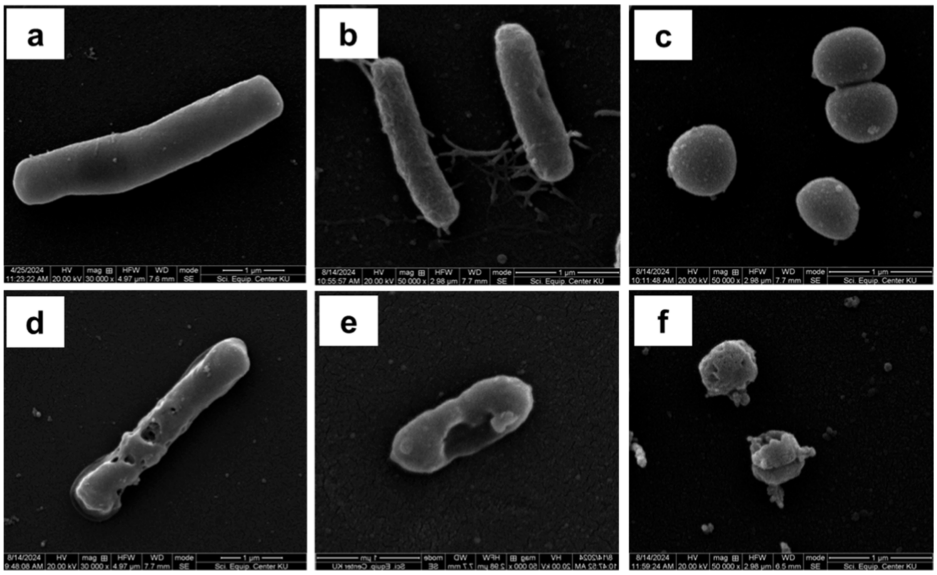

Figure 5. SEM images of (a) *Bacillus cereus*, (b) *E. coli*, and (c) *S. aureus* untreated and (d–f) treated with Li-GS NPs.

GS NPs and BG-GS NPs, where increasing amounts of gold led to the formation of larger particles with enhanced roughness of the surface, as summarized in Figure S5 and Table S4 in the Supporting Information.

All synthesized Li-Ag NPs and Li-GS NPs were thoroughly characterized using dynamic light scattering (DLS) and zeta potential measurements, as summarized in Table S4 in the Supporting Information. The average hydrodynamic diameters of PKS-Ag NPs, PRW-Ag NPs, and BG-Ag NPs were measured to be 5.27, 6.50, and 4.58 nm, respectively. These results confirm that the as-prepared Li-Ag NPs are within the nanoscale range, which is consistent with the transmission electron microscopy (TEM) observations. However, the hydrodynamic diameters obtained for Li-GS NPs deviated from the TEM results due to the irregular shapes and sizes caused by the formation of bimetallic nanoparticles. The size increase of the Li-GS NPs can be attributed to the rapid dissolution of Ag within the nanoparticle templates and the subsequent reformation of gold-dominant structures. For Li-GS NPs-1000, the particle morphology drastically altered due to the significant gold content, leading to a rapid replacement of silver by gold. This swift metal substitution caused the nanoparticles to form random, nonuniform shapes and sizes. The aggregation of smaller particles resulted in the formation of larger particles with a high rough surface, as depicted in Figure 4d. Moreover, the zeta potential measurements of all Li-Ag NP samples revealed a pronounced negative surface charge, affirming their colloidal stability. Specifically, PKS-Ag NPs, PRW-Ag NPs, and BG-Ag NPs demonstrated zeta potentials of −47.97 mV, −44.43 mV, and −37.83 mV, respectively. These values indicate strong electrostatic repulsion between particles, contributing to their stability in a suspension. Similarly, all Li-GS NS samples exhibited negative surface charges, confirming their colloidal stability as well, as outlined in Table S4 in the Supporting Information. Additionally, STEM-EDX mapping has been utilized to identify the atomic concentrations of gold and silver in PKS-GS NPs. As shown in Table S5, there is a noticeable increase in the atomic percentage of Au across the sample series. Notably, in PKS-GS NPs-100, the Au content increases from 44% to 100% in PKS-GSNPs-1000, while the Ag content decreases from 56% to 0% in PKS-GS NPs-1000. These findings serve to reinforce the successful synthesis of

https://doi.org/10.1021/acsanm.5c03025
ACS Appl. Nano Mater. 2025, 8, 17527−17539

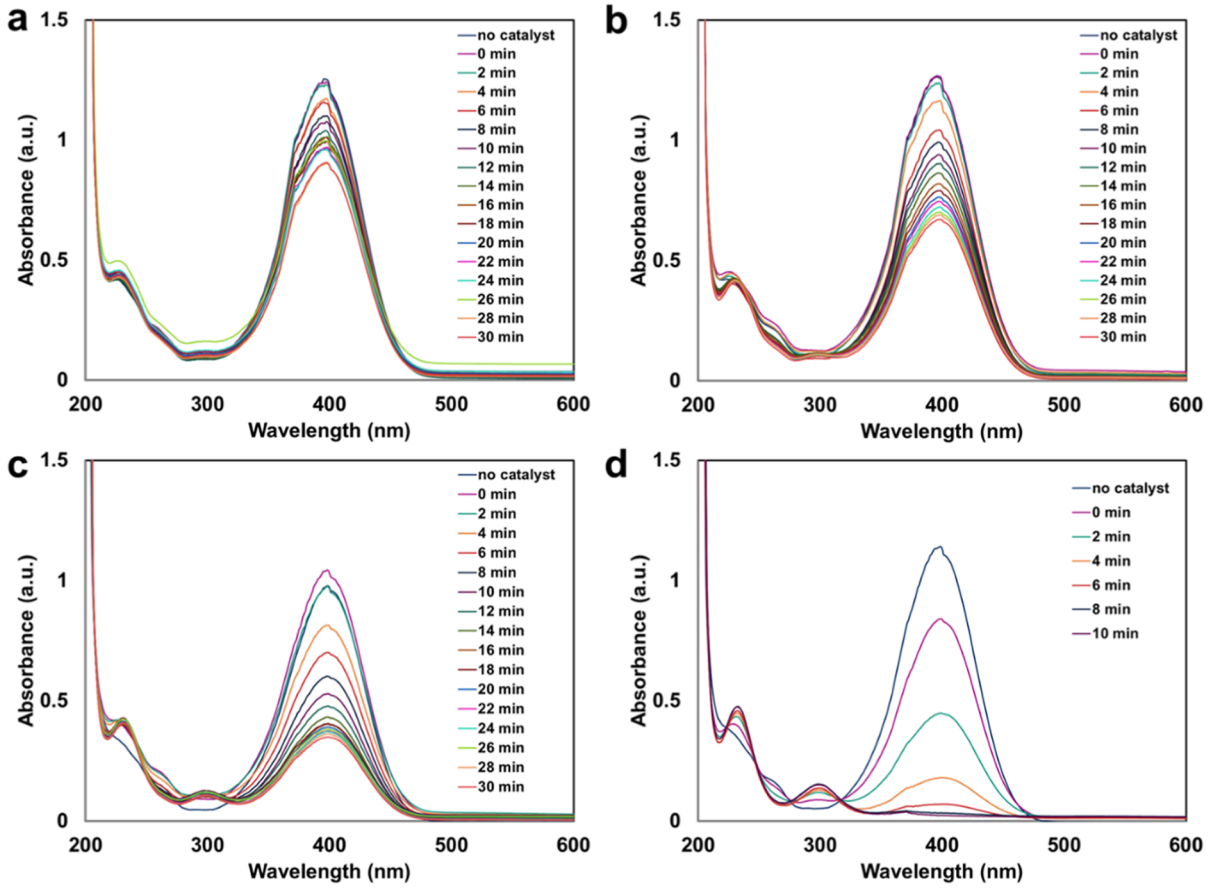

Figure 6. UV−visible absorption spectra of the catalytic conversion of 4-nitrophenol to 4-aminophenol (20 μL) using catalysts: (a) BG-GS NPs-100, (b) BG-GS NPs-300, (c) BG-GS NPs-500, and (d) BG-GS NPs-1000.

bimetallic PKS-GS NPs through this method, demonstrating a controllable synthesis process. Additionally, the STEM-EDS elemental mapping of PKS-GS NPs-500 and PKS-GS NPs-1000, presented in Figure S6 in the Supporting Information, confirmed a distribution of gold and silver, indicating the formation of Li-GS NPs in the alloy phase. Moreover, a comparative summary of reported green synthesis methods for bimetallic nanoparticles using various plant extracts is provided in the Supporting Information (Table S6), highlighting the advantages and limitations relative to this study.

3.4. Antibacterial Properties of Li-Ag NPs and Li-GS NPs. The antibacterial efficacy of all three Li-Ag NPs was assessed against Gram-positive *Bacillus cereus* and *Staphylococcus aureus* (*S. aureus*) and Gram-negative *Escherichia coli* (*E. coli*) as target bacteria. The results revealed that lignin exhibited no inhibition of bacterial growth across all tested concentrations, as summarized in Table S7. Conversely, the synthesized Li-Ag NPs demonstrated bacterial growth inhibition, with minimum inhibitory concentrations (MIC) at 20 μg/mL for all targeted bacteria. Additionally, minimum bactericidal concentration (MBC) tests were conducted by transferring samples from each well of microtiter plates onto Mueller Hinton Agar (MHA) plates, followed by incubation at 37 °C for 24 h. The results indicated that concentrations higher than 20 μg/mL for all targeted bacteria resulted in no visible growth on the MHA plates.

In the case of Li-GS NPs, the results show that all types of Li-GS NPs exhibit bacterial growth inhibition, with minimum inhibitory concentrations (MIC) ranging from 0.5 to 5 μg/mL for Gram-positive bacteria, including *Bacillus cereus* and *S. aureus*. The results indicated that the shape of bacteria does not have the effect on bacterial growth inhibition efficacy of the as-prepared nanoparticles. On the other hand, the MIC of Li-GS NPs on Gram-negative bacteria (*E. coli*) is in the range of 2.5 to 20 μg/mL, which is much higher than the MIC on Gram-positive bacteria. The MIC and MBC values of Li-Ag NPs and Li-GS NPs, summarized in Table 2, confirm that all Li-GS NPs samples have significant inhibition of bacterial growth against both Gram-positive and -negative bacteria at low concentrations. Additionally, scanning electron microscopy was employed to observe the physical morphology of the three bacterial strains. As shown in Figure 5, the results clearly indicate that the cell walls of all three bacterial species were damaged after treatment with Li-GS NPs. The bacterial cells exhibited disrupted and deformed structures, suggesting that Li-Ag NPs can effectively compromise the integrity of the bacterial cell envelope, leading to cell lysis or cell death. These morphological changes further support the strong antibacterial activity of Li-GS NPs observed in the MIC and MBC assays. For comparison, a detailed table of reported MIC values for bimetallic nanoparticles against various bacterial strains is provided in the Supporting Information (Table S8), highlighting the relative antibacterial performance of the present nanoparticles.

3.5. The Catalytic Activity of Li-Ag NPs and Li-GS NPs. The catalytic performance of Li-GS NPs was evaluated through the model reaction of 4-nitrophenol (4-NP) reduction to 4-aminophenol (4-AP). In this study, 10−30 μL of each catalyst

https://doi.org/10.1021/acsanm.5c03025
ACS Appl. Nano Mater. 2025, 8, 17527−17539

sample was employed. Upon addition of Li-GS NPs to the mixture of 4-NP and excess $NaBH_4$, a gradual fading of the characteristic yellow color was observed, indicating the progression of the reduction of 4-NP to 4-AP. This transformation was further confirmed by the steady decrease in absorbance at 400 nm as monitored by UV−visible spectroscopy, consistent with the depletion of 4-NP over time.[58,59] The results demonstrated that increasing the concentration of Au in the catalyst significantly enhanced the catalytic efficiency, leading to a shorter reaction time for the complete conversion of 4-NP to 4-AP, as illustrated in Figure 6. The comparison of catalytic performance is summarized in Table S9 in the Supporting Information.

Due to the large excess of $NaBH_4$ relative to 4-NP, the reaction follows pseudo-first-order kinetics with respect to 4-NP concentration. The kinetic plots for the catalytic reduction of 4-nitrophenol by $NaBH_4$ using the as-prepared nanoparticles are presented in Figures S7−S9, with the corresponding rate constants summarized in Table S10 of the Supporting Information. Among the tested PRW-GS NPs, the catalyst prepared with 1000 μL of $KAuCl_4$ exhibited the highest catalytic efficiency with the apparent rate constant (k_{app}) = 2.618 min^{-1}. The reaction was so rapid completing in less than one min that it was not possible to collect enough absorbance data to construct a reliable kinetic plot or determine an accurate rate constant. Catalysts prepared with lower volumes of $KAuCl_4$ showed progressively lower rate constants, indicating that the gold content strongly influences the reduction rate via enhanced surface reactivity and Au−Ag synergy.

To further understand the influence of lignin type on catalytic behavior, the apparent rate constants of GS NPs synthesized from different lignin sources, bagasse (BG), palm kernel shell (PKS), and pararubber wood (PRW) were compared. For BG-GS NPs, the k_{app} values gradually increased from 0.0097 to 0.0513 min^{-1} as $KAuCl_4$ volume increased from 100 to 1000 μL, suggesting a dose-dependent improvement in catalytic performance due to enhanced bimetallic interface formation. In contrast, PKS-GS NPs displayed a nonlinear trend; although 500 μL gave the highest rate constant (0.428 min^{-1}), the catalytic activity dropped at 1000 μL (0.3345 min^{-1}), indicating possible nanoparticle overgrowth or agglomeration at higher gold loading. Notably, even at 100 μL, PKS-GS NPs showed a relatively high-rate constant (0.1443 min^{-1}), likely due to the lignin's high phenolic content promoting rapid initial nucleation. For PRW-GS NPs, the trend was more linear, with k_{app} increasing from 0.0108 to 0.352 min^{-1} between 100 and 500 μL, highlighting the role of aliphatic groups in promoting dispersion and stability. These results demonstrate that both the volume of $KAuCl_4$ and the functional group composition of lignin significantly influence the catalytic performance. The balance between gold content, particle dispersion, and lignin−metal interaction plays a key role in determining the final efficiency of GS NPs as catalysts for the reduction of 4-NP to 4-AP.

Additionally, the catalytic results clearly showed that increasing the volume of the catalyst enhanced the reaction efficiency. Specifically, higher volumes of Li-GS NPs led to faster reaction rates compared with the lower volume. Among them, PRW-GS NPs at a volume of 30 μL exhibited the highest catalytic efficiency, completing the reaction in just a few minutes, whereas BG-GS NPs and PKS-GS NPs took approximately 10 min to achieve the same conversion, as illustrated in Figure S10 in the Supporting Information. This improved performance at higher catalyst volumes is primarily due to the increased number of active surface sites available for the reaction. With a greater quantity of nanoparticles in the system, there is an enhanced availability of surface-bound electrons to facilitate electron transfer from the reducing agent ($NaBH_4$) to the 4-NP molecules. This accelerates the reduction process and significantly reduces the overall reaction time. Furthermore, better dispersion of the catalyst in the reaction medium at higher volumes promotes more effective interaction between the catalyst and the substrate.[60] These observations underscore the importance of catalyst dosage in influencing the catalytic performance, suggesting that an optimal amount of catalyst can greatly enhance both the rate and efficiency of the reaction.

This enhancement in catalytic activity is attributed to the synergistic effect between Au and Ag atoms, the increased surface area of nanoparticles, and improved electron transfer capabilities.[61] Therefore, the catalytic performance improves significantly with increased catalyst volume and optimized nanoparticle size, demonstrating that both the composition and dosage play crucial roles in accelerating the reduction reaction. The results clearly demonstrate that both particle size and bimetallic composition play critical roles in optimizing the catalytic performance for environmental and industrial applications.

4. CONCLUSION

The study characterized lignin samples from three different sources, including BG, PRW, and PKS, using ^{31}P NMR spectroscopy, which revealed variations in their hydroxyl group compositions. These differences in hydroxyl group types and contents may influence the synthesis rate of Li-Ag NPs due to variations in electron donation capabilities. The synthesis of Li-Ag NPs was successfully achieved using lignin as a reducing agent, confirmed by UV−visible spectroscopy, which identified characteristic Ag NP peaks at 420 nm. Additionally, Li-GS NPs were synthesized using Li-Ag NPs as templates, with the optimization of reaction conditions indicating that a 24 h reaction time yielded the most significant change in optical properties. TEM images of the as-prepared nanoparticles confirmed the nanoscale dimensions of Li-Ag NPs and the diverse shapes of Li-GS NPs. Dynamic light scattering (DLS) and zeta potential measurements confirmed the nanoscale size and colloidal stability of both Li-Ag NPs and Li-GS NPs. STEM-EDX mapping revealed the successful synthesis of bimetallic Li-GS NPs, with varying atomic concentrations of gold and silver across different samples, indicative of a controllable synthesis process. Finally, the antibacterial properties of Li-Ag NPs and Li-GS NPs were evaluated against *Bacillus cereus*, *E. coli*, and *S. aureus* demonstrating significant growth inhibition at low concentrations of Li-GS NPs, as evidenced by minimum inhibitory concentration (MIC) and minimum bactericidal concentration (MBC) tests. The results confirmed that all Li-GS NPs had better antibacterial efficacy compared to Li-Ag NPs. In addition, the catalytic performance of Li-Ag NPs and Li-GS NPs was investigated. It was found that the Li-GS NPs with the highest gold content exhibited the highest catalytic activity in promoting the conversion of 4-nitrophenol to 4-aminophenol. This enhanced activity is attributed to the rough surface morphology resulting from the etching and reassembly of the synthesized nanoparticles. Overall, this study confirms that lignin from agricultural waste

https://doi.org/10.1021/acsanm.5c03025
ACS Appl. Nano Mater. 2025, 8, 17527−17539

can serve as a sustainable and efficient platform for synthesizing multifunctional nanomaterials. By selecting appropriate lignin sources and optimizing synthesis parameters, the resulting Li-GS NPs can be tailored for specific optical, antimicrobial, and catalytic applications. This approach not only minimizes environmental impact but also contributes to the valorization of biomass residues.

■ ASSOCIATED CONTENT

Supporting Information

The Supporting Information is available free of charge at https://pubs.acs.org/doi/10.1021/acsanm.5c03025.

Additional details on absorption spectra of lignin solutions and nanoparticles, maximum absorbance wavelengths and NMR chemical shifts of lignin functional groups, chemical structures of lignin hydroxyl groups, TEM and STEM-EDX images of nanoparticles synthesized with varying lignin concentrations and $KAuCl_4$ volumes, FTIR spectra of lignin and Li-Ag NPs, particle size, zeta potential, and elemental composition data of synthesized nanoparticles, antibacterial activity and comparison with reported green synthesis methods, and catalytic performance and kinetics data for 4-nitrophenol reduction (PDF)

■ AUTHOR INFORMATION

Corresponding Author

Pannaree Srinoi − *Department of Chemistry, Faculty of Science, Kasetsart University, Bangkok 10900, Thailand; Department of Chemistry and Center of Excellence for Innovation in Chemistry, Faculty of Science, Kasetsart University, Bangkok 10900, Thailand;* orcid.org/0000-0003-4400-468X; Email: pannaree.sr@ku.th

Authors

Punsachon Jaroensin − *Department of Chemistry, Faculty of Science, Kasetsart University, Bangkok 10900, Thailand*

Janistar Nunsap − *Department of Chemistry, Faculty of Science, Kasetsart University, Bangkok 10900, Thailand*

Vipada Khuanchom − *Department of Chemistry, Faculty of Science, Kasetsart University, Bangkok 10900, Thailand*

Bongkot Hararak − *National Metal and Materials Technology Center, National Science and Technology Development Agency, Thailand Science Park, Pathum Thani 12120, Thailand;* orcid.org/0000-0002-7143-9614

Piyangkun Lueangjaroenkit − *Department of Microbiology, Faculty of Science, Kasetsart University, Bangkok 10900, Thailand; Biodiversity Center Kasetsart University (BDCKU), Bangkok 10900, Thailand*

Tawan Sooknoi − *Department of Chemistry, Faculty of Science, King Mongkut's Institute of Technology Ladkrabang, Bangkok 10520, Thailand;* orcid.org/0000-0002-3874-0384

T. Randall Lee − *Department of Chemistry and the Texas Center for Superconductivity, University of Houston, Houston, Texas 77204-5003, United States;* orcid.org/0000-0001-9584-8861

Complete contact information is available at: https://pubs.acs.org/10.1021/acsanm.5c03025

Author Contributions

P.S. was responsible for conceptualization, data curation, project administration, and editing. T.R.L. and T.S. were responsible for supervision and funding acquisition. V.K. and B.H. were responsible for lignin preparation and characterizations. V.K., J.N., and P.J. were responsible for synthesis and investigations of nanoparticles. P.L., P.J., and J.N. were responsible for antibacterial methods. P.J. was responsible for visualization, writing, and review.

Notes

The authors declare no competing financial interest.

■ ACKNOWLEDGMENTS

This project is funded by (1) the National Research Council of Thailand (NRCT) and Kasetsart University (N42A660822) and (2) Kasetsart University through the Graduate School Fellowship Program. The research was also supported by Kasetsart University Research and Development Institute, KURDI (grant no. FF(KU-SRIU)3.67) and Center of Excellence for Innovation in Chemistry.

■ REFERENCES

(1) Klębowski, B.; Depciuch, J.; Parlińska-Wojtan, M.; Baran, J. Applications of Noble Metal-Based Nanoparticles in Medicine. *Int. J. Mol. Sci.* **2018**, *19* (12), 4031.

(2) Baig, N.; Kammakakam, I.; Falath, W. Nanomaterials: A Review of Synthesis Methods, Properties, Recent Progress, and Challenges. *Mater. Adv.* **2021**, *2* (6), 1821−1871.

(3) Capek, I. *Noble Metal Nanoparticles: Preparation, Composite Nanostructures, Biodecoration and Collective Properties*, 1st ed.; Springer: Tokyo, Japan, 2017.

(4) Zhang, Z.; Lin, P.-C. Noble Metal Nanoparticles: Synthesis, and Biomedical Implementations. *Emerging Applications of Nanoparticles and Architecture Nanostructures*; Elsevier, 2018; pp 177−233.

(5) Medina-Cruz, D.; Saleh, B.; Vernet-Crua, A.; Nieto-Argüello, A.; Lomelí-Marroquín, D.; Vélez-Escamilla, L. Y.; Cholula-Díaz, J. L.; García-Martín, J. M.; Webster, T. Bimetallic Nanoparticles for Biomedical Applications: A Review. *Racing for the Surface*; Springer International Publishing: Cham, 2020; pp 397−434.

(6) Srinoi, P.; Chen, Y.-T.; Vittur, V.; Marquez, M. D.; Lee, T. R. Bimetallic Nanoparticles: Enhanced Magnetic and Optical Properties for Emerging Biological Applications. *Appl. Sci. (Basel)* **2018**, *8* (7), 1106.

(7) Padre, S. M.; Kiruthika, S.; Mundinamani, S.; Ravikirana; Surabhi, S.; Jeong, J.-R.; Eshwarappa, K. M.; Murari, M. S.; Shetty, V.; Ballal, M.; Gurumurthy, S. C. Mono- and Bimetallic Nanoparticles for Catalytic Degradation of Hazardous Organic Dyes and Antibacterial Applications. *ACS Omega* **2022**, *7* (39), 35023−35034.

(8) Meher, A.; Tandi, A.; Moharana, S.; Chakroborty, S.; Mohapatra, S. S.; Mondal, A.; Dey, S.; Chandra, P. Silver Nanoparticle for Biomedical Applications: A Review. *Hybrid Adv.* **2024**, *6*, 100184.

(9) Sati, A.; Ranade, T. N.; Mali, S. N.; Ahmad Yasin, H. K.; Pratap, A. Silver Nanoparticles (AgNPs): Comprehensive Insights into Bio/Synthesis, Key Influencing Factors, Multifaceted Applications, and Toxicity-A 2024 Update. *ACS Omega* **2025**, *10* (8), 7549−7582.

(10) Shah, M. Gold Nanoparticles: Various Methods of Synthesis and Antibacterial Applications. *Front. Biosci.* **2014**, *19* (8), 1320.

(11) Marcelino, M. Y.; Borges, F. A.; Scorzoni, L.; de Lacorte Singulani, J.; Garms, B. C.; Niemeyer, J. C.; Guerra, N. B.; Pegorin Brasil, G. S.; Mussagy, C. U.; de Oliveira Carvalho, F. A.; Scontri, M.; Mendes-Giannini, M. J. S.; Fusco-Almeida, A. M.; Herculano, R. D. Synthesis and Characterization of Gold Nanoparticles and Their Toxicity in Alternative Methods to the Use of Mammals. *J. Environ. Chem. Eng.* **2021**, *9* (6), 106779.

(12) Zhang, J.; Mou, L.; Jiang, X. Surface Chemistry of Gold Nanoparticles for Health-Related Applications. *Chem. Sci.* **2020**, *11* (4), 923−936.
(13) Diem, P. N. H.; Phuong, T. N. M.; Hien, N. Q.; Quang, D. T.; Hoa, T. T.; Cuong, N. D. Silver, Gold, and Silver-Gold Bimetallic Nanoparticle-Decorated Dextran: Facile Synthesis and Versatile Tunability on the Antimicrobial Activity. *J. Nanomater.* **2020**, *2020*, 1−11.
(14) Iravani, S.; Korbekandi, H.; Mirmohammadi, S. V.; Zolfaghari, B. Synthesis of Silver Nanoparticles: Chemical, Physical and Biological Methods. *Res. Pharm. Sci.* **2014**, *9* (6), 385−406.
(15) Mladenova, B.; Stankulov, T.; Stankov, S.; Karsheva, M.; Hinkov, I.; Momchilov, A.; Boukoureshtlieva, R. Sonochemical Synthesis of Silver Nanoparticles for Gas-Diffusion Electrodes Application. *J. Chem. Technol. Met.* **2024**, *59* (5), 1119−1129.
(16) Ying, S.; Guan, Z.; Ofoegbu, P. C.; Clubb, P.; Rico, C.; He, F.; Hong, J. Green Synthesis of Nanoparticles: Current Developments and Limitations. *Environ. Technol. Innovation* **2022**, *26*, 102336.
(17) Liu, T.; Baek, D. R.; Kim, J. S.; Joo, S.-W.; Lim, J. K. Green Synthesis of Silver Nanoparticles with Size Distribution Depending on Reducing Species in Glycerol at Ambient pH and Temperatures. *ACS Omega* **2020**, *5* (26), 16246−16254.
(18) Luo, P.; Feng, X.; Liu, S.; Jiang, Y. Traditional Uses, Phytochemistry, Pharmacology and Toxicology of Ruta Graveolens L.: A Critical Review and Future Perspectives. *Drug Des., Dev. Ther.* **2024**, *18*, 6459−6485.
(19) Khalid, Z.; Ali, A.; Siddique, A. B.; Zaman, Y.; Sibtain, M. F.; Abbas, A.; Alam, M. M.; Alwethaynani, M. S. Causonis Trifolia-Based Green Synthesis of Multifunctional Silver Nanoparticles for Dual Sensing of Mercury and Ferric Ions, Photocatalysis, and Biomedical Applications. *RSC Adv.* **2025**, *15* (21), 16879−16893.
(20) Ray, S. K.; Bhuiyan, R. H.; Muslim, T.; Ehsan, M. Q. Development of a Material-Driven Phase III Lignocellulosic Feedstock Biorefinery System. *ACS Sustainable Resour. Manage.* **2024**, *1* (9), 1994−2013.
(21) Mujtaba, M.; Fernandes Fraceto, L.; Fazeli, M.; Mukherjee, S.; Savassa, S. M.; Araujo de Medeiros, G.; do Espírito Santo Pereira, A.; Mancini, S. D.; Lipponen, J.; Vilaplana, F. Lignocellulosic Biomass from Agricultural Waste to the Circular Economy: A Review with Focus on Biofuels, Biocomposites and Bioplastics. *J. Cleaner Prod.* **2023**, *402*, 136815.
(22) Ashokkumar, V.; Venkatkarthick, R.; Jayashree, S.; Chuetor, S.; Dharmaraj, S.; Kumar, G.; Chen, W.-H.; Ngamcharussrivichai, C. Recent Advances in Lignocellulosic Biomass for Biofuels and Value-Added Bioproducts—A Critical Review. *Bioresour. Technol.* **2022**, *344*, 126195.
(23) Zhang, L.; Larsson, A.; Moldin, A.; Edlund, U. Comparison of Lignin Distribution, Structure, and Morphology in Wheat Straw and Wood. *Ind. Crops Prod.* **2022**, *187*, 115432.
(24) Obrzut, N.; Hickmott, R.; Shure, L.; Gray, K. A. The Effects of Lignin Source and Extraction on the Composition and Properties of Biorefined Depolymerization Products. *RSC Sustainability* **2023**, *1* (9), 2328−2340.
(25) Heo, J. W.; Oh, D. H.; Xia, Q.; Kim, M. S.; Kim, Y. S. Green Synthesis of Silver Nanoparticles-Capped Aminated Lignin as a Robust Active Catalyst for Dye Discoloration. *Int. J. Biol. Macromol.* **2024**, *274*, 133211.
(26) Li, Y.; Yang, D.; Li, P.; Li, Z. Lignin as a Multi-Functional Agent for the Synthesis of Ag Nanoparticles and Its Application in Antibacterial Coatings. *J. Mater. Res. Technol.* **2022**, *17*, 3211−3220.
(27) Wang, B.; Yang, G.; Chen, J.; Fang, G. Green Synthesis and Characterization of Gold Nanoparticles Using Lignin Nanoparticles. *Nanomaterials (Basel)* **2020**, *10* (9), 1869.
(28) Morena, A. G.; Tzanov, T. Antibacterial Lignin-Based Nanoparticles and Their Use in Composite Materials. *Nanoscale Adv.* **2022**, *4* (21), 4447−4469.
(29) Khantamat, O.; Li, C.-H.; Yu, F.; Jamison, A. C.; Shih, W.-C.; Cai, C.; Lee, T. R. Gold Nanoshell-Decorated Silicone Surfaces for the near-Infrared (NIR) Photothermal Destruction of the Pathogenic Bacterium E. Faecalis. *ACS Appl. Mater. Interfaces* **2015**, *7* (7), 3981−3993.
(30) Kuppusamy, P.; Kim, S.; Kim, S.-J.; Song, K.-D. Antimicrobial and Cytotoxicity Properties of Biosynthesized Gold and Silver Nanoparticles Using D. Brittonii Aqueous Extract. *Arabian J. Chem.* **2022**, *15* (11), 104217.
(31) Liu, Y.; Wang, Y.; Fu, Y.; Wang, N.; Liu, Q.; Zhao, S.; Yang, H. Y.; Liu, C. Fabrication of Temperature and pH Dual-Sensitive Semi-Interpenetrating Network Hydrogel with Enhanced Adhesion and Antibacterial Properties. *Polymer* **2025**, *326*, 128343.
(32) Yang, H.; Wang, X.; Wang, J.; Liu, H.; Jin, H.; Zhang, J.; Li, G.; Tang, Y.; Ye, C. High-Value Utilization of Agricultural Waste: A Study on the Catalytic Performance and Deactivation Characteristics of Iron-Nickel Supported Biochar-Based Catalysts in the Catalytic Cracking of Toluene. *Energy* **2025**, *323*, 135806.
(33) Siddique, A. B.; Shaheen, M. A.; Abbas, A.; Zaman, Y.; Amin, H. M. A.; Alam, M. M.; Alharbi, N. K.; Alshehri, F.; Shami, A.; Al-Joufi, F. A.; Ali, A. Sunlight-assisted greenly synthesised silver nanoparticles for highly selective mercury ion sensing, biomedical and photocatalytic applications. *Int. J. Environ. Anal. Chem.* **2025**, 1−23.
(34) Xu, R.; Liao, L.; Liang, W.; Wang, H.; Zhou, Q.; Liu, W.; Chen, M.; Fang, B.; Wu, D.; Jin, H.; Li, Y.; Zou, S.; Lu, L. Fast Removing Ligands from Platinum-Based Nanocatalysts by a Square-Wave Potential Strategy. *Angew. Chem., Int. Ed. Engl.* **2025**, *64* (32), No. e202509746.
(35) Kanwal, M.; Sher, M.; Abbas, A.; Akhtar, S.; Siddique, A. B.; Naeem ul Hasan, M.; Assad, N.; Alhazmi, H. A.; Amin, H. M. A. Dual Colorimetric Sensing of Hg(II) and Fe(III) Using Sulfanilamide-Stabilized Silver Nanoparticles and Evaluating Their Photodegradation and Antibacterial Properties. *J. Water Proc. Eng.* **2025**, *75*, 107981.
(36) Schneider, W. D. H.; Dillon, A. J. P.; Camassola, M. Lignin Nanoparticles Enter the Scene: A Promising Versatile Green Tool for Multiple Applications. *Biotechnol. Adv.* **2021**, *47*, 107685.
(37) Pongchaiphol, S.; Suriyachai, N.; Hararak, B.; Raita, M.; Laosiripojana, N.; Champreda, V. Physicochemical Characteristics of Organosolv Lignins from Different Lignocellulosic Agricultural Wastes. *Int. J. Biol. Macromol.* **2022**, *216*, 710−727.
(38) Tippayawat, P.; Phromviyo, N.; Boueroy, P.; Chompoosor, A. Green Synthesis of Silver Nanoparticles in Aloe Vera Plant Extract Prepared by a Hydrothermal Method and Their Synergistic Antibacterial Activity. *PeerJ* **2016**, *4*, No. e2589.
(39) Berahim, N.; Basirun, W. J.; Leo, B. F.; Johan, M. R. Synthesis of Bimetallic Gold-Silver (Au-Ag) Nanoparticles for the Catalytic Reduction of 4-Nitrophenol to 4-Aminophenol. *Catalysts* **2018**, *8* (10), 412.
(40) Calvo-Flores, F. G. Lignin: A Renewable Raw Material. *Encyclopedia of Renewable and Sustainable Materials*; Elsevier, 2020; pp 102−118.
(41) Schutyser, W.; Renders, T.; Van den Bosch, S.; Koelewijn, S.-F.; Beckham, G. T.; Sels, B. F. Chemicals from Lignin: An Interplay of Lignocellulose Fractionation, Depolymerisation, and Upgrading. *Chem. Soc. Rev.* **2018**, *47* (3), 852−908.
(42) Xin, X.; Qi, C.; Xu, L.; Gao, Q.; Liu, X. Green Synthesis of Silver Nanoparticles and Their Antibacterial Effects. *Front. Chem. Eng.* **2022**, *4*, 941240.
(43) Crestini, C.; Melone, F.; Sette, M.; Saladino, R. Milled Wood Lignin: A Linear Oligomer. *Biomacromolecules* **2011**, *12* (11), 3928−3935.
(44) Liu, K.; Du, H.; Zheng, T.; Liu, W.; Zhang, M.; Liu, H.; Zhang, X.; Si, C. Lignin-Containing Cellulose Nanomaterials: Preparation and Applications. *Green Chem.* **2021**, *23* (24), 9723−9746.
(45) Inkrod, C.; Raita, M.; Champreda, V.; Laosiripojana, N. Characteristics of Lignin Extracted from Different Lignocellulosic Materials via Organosolv Fractionation. *Bioenergy Res.* **2018**, *11* (2), 277−290.
(46) Maršík, D.; Danda, M.; Otta, J.; Thoresen, P. P.; Mat Átková, O.; Rova, U.; Christakopoulos, P.; Matsakas, L.; Masák, J. Preparation

https://doi.org/10.1021/acsanm.5c03025
ACS Appl. Nano Mater. 2025, 8, 17527−17539

and Biological Activity of Lignin-Silver Hybrid Nanoparticles. *ACS Omega* **2024**, *9* (48), 47765−47787.
(47) Sun, X.-F.; Jing, Z.; Fowler, P.; Wu, Y.; Rajaratnam, M. Structural Characterization and Isolation of Lignin and Hemicelluloses from Barley Straw. *Ind. Crops Prod.* **2011**, *33* (3), 588−598.
(48) Chen, S.; Wang, G.; Sui, W.; Parvez, A. M.; Si, C. Synthesis of Lignin-Functionalized Phenolic Nanosphere Supported Ag Nanoparticles with Excellent Dispersion Stability and Catalytic Performance. *Green Chem.* **2020**, *22* (9), 2879−2888.
(49) Ito, N. M.; de Andrade Mendes Filho, A.; dos Santos, D. J.; dos Santos, L. T. Synthesis of Silver Nanoparticles Using Modified Lignin as a Reducing Agent. *Next Mater.* **2024**, *2*, 100101.
(50) Manisekaran, A.; Grysan, P.; Duez, B.; Schmidt, D. F.; Lenoble, D.; Thomann, J.-S. Solvents Drive Self-Assembly Mechanisms and Inherent Properties of Kraft Lignin Nanoparticles (<50 Nm). *J. Colloid Interface Sci.* **2022**, *626*, 178−192.
(51) Purbowati, R.; Kirana, O. S. S.; Rozafia, A. I.; Utomo, W. P.; Rosyidah, A.; Taufikurohmah, T.; Syahrani, A.; Hartanto, D. Green Synthesis of One-Dimensional Silver Nanoparticles Using Quercus Infectoria Gall Extract. *Case Stud. Chem. Environ. Eng.* **2024**, *9*, 100728.
(52) Zhang, X.-F.; Liu, Z.-G.; Shen, W.; Gurunathan, S. Silver Nanoparticles: Synthesis, Characterization, Properties, Applications, and Therapeutic Approaches. *Int. J. Mol. Sci.* **2016**, *17* (9), 1534.
(53) Krishnamurthy, S.; Esterle, A.; Sharma, N. C.; Sahi, S. V. Yucca-Derived Synthesis of Gold Nanomaterial and Their Catalytic Potential. *Nanoscale Res. Lett.* **2014**, *9* (1), 627.
(54) Xie, X.; van Huis, M. A.; van Blaaderen, A. Morphology-Controlled Growth of Crystalline Ag-Pt-Alloyed Shells onto Au Nanotriangles and Their Plasmonic Properties. *J. Phys. Chem. C Nanomater. Interfaces* **2023**, *127* (32), 16052−16060.
(55) Salem, W. M.; Haridy, M.; Sayed, W. F.; Hassan, N. H. Antibacterial Activity of Silver Nanoparticles Synthesized from Latex and Leaf Extract of Ficus Sycomorus. *Ind. Crops Prod.* **2014**, *62*, 228−234.
(56) Sirgedaite, G.; Talaikis, M.; Drabavicius, A.; Niaura, G.; Mikoliunaite, L. Synthesis and Characterization of Au@Ag Nanoparticles for Multiwavelength SERS Biosensing. *Spectrochim. Acta, Part A* **2025**, *338*, 126160.
(57) Traoré, N. E.; Spruck, C.; Uihlein, A.; Pflug, L.; Peukert, W. Targeted Color Design of Silver-Gold Alloy Nanoparticles. *Nanoscale Adv.* **2024**, *6* (5), 1392−1408.
(58) Mata, R.; Reddy Nakkala, J.; Rani Sadras, S. Catalytic and Biological Activities of Green Silver Nanoparticles Synthesized from Plumeria Alba (Frangipani) Flower Extract. *Mater. Sci. Eng. C Mater. Biol. Appl.* **2015**, *51*, 216−225.
(59) Wunder, S.; Lu, Y.; Albrecht, M.; Ballauff, M. Catalytic Activity of Faceted Gold Nanoparticles Studied by a Model Reaction: Evidence for Substrate-Induced Surface Restructuring. *ACS Catal.* **2011**, *1* (8), 908−916.
(60) Fang, J.; Xu, X.; Yang, Y.; Han, Z.; Zuo, Z.; Han, W.; Lin, B. An integrated ZnO−SnO_2 n−n heterostructure strategy of catalysts and ash for promoting diesel soot combustion. *J. Therm. Anal. Calorim.* **2025**, *150*, 7335−7347.
(61) Zhang, Y.; Sun, M. Ag-Au Bimetallic Nanoparticle-Based Electrochemical Sensing Platform for Quantification of B-Type Natriuretic Peptide. *Int. J. Electrochem. Sci.* **2024**, *19* (8), 100703.

https://doi.org/10.1021/acsanm.5c03025
ACS Appl. Nano Mater. 2025, 8, 17527−17539